Optics Communications 285 (2012) 5306–5312

Contents lists available at SciVerse ScienceDirect

Optics Communications

journal homepage: www.elsevier.com/locate/optcom

Theoretical analysis of off beam quartz-enhanced photoacoustic spectroscopy sensor

Hongming Yi [a,b], Kun Liu [a,b], Shanwen Sun [a,b], Weijun Zhang [a,b], Xiaoming Gao [a,b,*]

[a] Key Laboratory of Atmospheric Composition and Optical Radiation, Chinese Academy of Science, Hefei 230031, China
[b] Laboratory of Atmospheric Physico-Chemistry, Anhui Institute of Optics and Fine Mechanics, Chinese Academy of Sciences, Hefei 230031, China

ARTICLE INFO

Article history:
Received 23 February 2012
Received in revised form
15 May 2012
Accepted 15 July 2012
Available online 13 August 2012

Keywords:
Theoretical model
Off beam quartz-enhanced photoacoustic spectroscopy
Microresonator

ABSTRACT

Off beam quartz-enhanced photoacoustic spectroscopy (OB-QEPAS) sensors are based on a recently developed approach to off-beam photoacoustic (PA) detection which employs a quartz tuning fork (QTF) as an acoustic transducer. A microresonator (mR) with a side slit in the middle is used to enhance PA signal. This paper describes a theoretical model of an OB-QEPAS-based sensor. By deriving the acoustic impedances of the mR at two ends and the side slit in the middle in the model, we obtain a formula for numerically calculating the optimal mRs' parameters of OB-QEPAS-based sensor. We use the model to calculate the optimal mRs' lengths with respect to the resonant frequency of the QTF, acoustic velocities inside mRs, inner diameters of mRs, and acoustic conductivities of the mRs' side slits, and found out that the calculated results closely match experimental data. We also investigated the relationship between the mR selected in "on beam" QEPAS, OB-QEPAS, and an acoustic resonator (AR) excited in its first longitudinal mode used in conventional photoacoustic spectroscopy (PAS).

1. Introduction

Laser photoacoustic spectroscopy (PAS) [1,2] is a well established method used in trace gas sensing applications, which is based on detecting acoustic waves generated by a medium absorbing modulated optical radiation as a result of photoacoustic (PA) effect. A sensitive acoustic transducer is used to detect PA signal. Up to date, due to the alternative acoustic transducers, broadband microphone based conventional PAS [3], quartz-enhanced PAS (QEPAS) [4], micro electro-mechanical systems (MEMS) scaled PAS (MEMS-scale PAS) [5], newly developed PAS used electromechanical films (EMFIT) as acoustic transducer (EMFIT based PAS) [6] and silicon cantilever enhanced PAS [7] have been demonstrated and widely used for trace gas detection. Actually, our research purpose is to acquire higher sensitivity and more compact system configuration of PAS-based sensor. As a result, research committed to further improve the sensitivity of PAS-based sensor has followed schematically three lines: use of new light sources, design of different resonant cell types with optimized geometry, and improvement of data analysis. In particular, designing optimum resonant PA cells in traditional PAS to improve the signal to noise ratio (SNR) was verified to be a very effective method through the former theoretical analysis and experiments measurements [8–12]. Conventional microphone based PAS with optimized resonant PA cell has been acquired very high sensitivity and employed to widespread applications [1–3,8–12].

Quartz-enhanced photoacoustic spectroscopy (QEPAS) is a newly developed sensor technology which firstly introduced by A.A. Kosterv in 2002 [13]. In combination with various light sources, such as diode laser or laser diode (DL or LD), optical parametric oscillators (OPO), interband cascade lasers (ICLs) and quantum cascade lasers (QCLs), QEPAS has been successfully applied to the detection of various simple molecules with narrow absorption spectra [14–16] and larger molecules with broad, unresolved spectral absorption features [17–19]. Analogous to traditional microphone based PAS, it is a very effective method to design and optimize acoustic microresonator (mR) for further improving the sensitivity of QEPAS-based trace gas sensor [20,21]. As a result, recently, four typical QEPAS spectrophones configurations [21] have been reported, which referred to "bare QTF QEPAS", on beam QEPAS, half on beam QEPAS, and off beam QEPAS (OB-QEPAS), respectively. The reported OB-QEPAS-based sensor configurations include a spectrophone (the module for detecting laser-induced sound) consisting of a QTF and a microresonator composed of a tube with a side slit in the middle [22,23]. Experiments have shown that OB-QEPAS yields a SNR gain ~19 compared to "bare QTF QEPAS" [23]. But for on beam QEPAS with the optimum mR parameters, its SNR gain can be as high as ~30 compared to "bare QTF QEPAS" [16,20,21]. Comparing the SNR gain of OB-QEPAS to that of on-beam QEPAS

* Corresponding author at: Chinese Academy of Science, Key Laboratory of Atmospheric Composition and Optical Radiation, Hefei 230031, China.
Tel./fax: +86 551 5591534.
E-mail address: xmgao@aiofm.ac.cn (X. Gao).

0030-4018/$ - see front matter © 2012 Elsevier B.V. All rights reserved.
http://dx.doi.org/10.1016/j.optcom.2012.07.056

spectrophone design, the optimum OB-QEPAS design has a 1.6–1.7 weaker SNR gain at atmospheric pressure [23]. However, technologically, OB-QEPAS is more flexible, easier to assemble and align regarding configurations between QTF and mR, as the excited light source no more pass through the smaller gap between the prongs but directly through the mR to avoid obstruction of the used excitation radiation. Especially, for real application, OB-QEPAS spectrophone design makes it possible to have the advantage to use light sources with lower beam quality. For example, broadband blue laser diode based OB-QEPAS was developed for trace NO_2 detection [19], light emitted diode was used as excited source for O_3 measurements with OB-QEPAS [24], and OB-QEPAS was adopted to measure the alignment-dependent energy dumped into gaseous linear molecules (O_2, N_2, CO_2 and CO) [25]. Those examples all used light sources with low beam quality as PA excited sources. These advantages make OB-QEPAS spectrophone configuration to become as important as "on beam" structure. However, former works [22,23] mainly focused on experimental study and the systematical theory for OB-QEPAS was not given. So that it is necessary to analyze OB-QEPAS spectrophone theoretically for designing and optimizing OB-QEPAS-based sensor.

In this paper, we describe a theoretical model for OB-QEPAS-based sensor currently proposed by Kun Liu et al. [22,23]. This theoretical model was used to calculate the optimum mR lengths with respect to different acoustic velocities, various inner diameters (IDs), outer diameters (ODs) and the side slits of mRs. The model was validated by comparison theoretical calculations with experimental results cited from [22,23]. Our model shows that the theoretical calculations and experimental measurements are in very good agreement. The influence of acoustic velocity on OB-QEPAS-based sensor performance was also investigated. Finally, the relationship between the mR used in OB-QEPAS and on beam QEPAS and acoustic resonator (AR) excited in its first longitudinal mode adopted in conventional microphone based PAS was analyzed and discussed.

2. Theoretical model

OB-QEPAS spectrophone consists of a QTF and a so-called mR (shown in Fig. 1(a) and 1(b)). The mR is formed by one tube with a side slit in the middle (shown in Fig. 1(c)), and the QTF is coupled to the mR by putting it outside the mR tube near the opening of the side slit to probe the acoustic vibration excited in the gas contained inside the tube [22,23] (shown in Fig. 1(a) and 1(b)). Being different from conventional microphone with response frequency of 20–20,000 Hz, the QTF is used as an acoustic transducer with a fixed response frequency of $f_0 \sim 32.768$ kHz, and the mR with a side slit in the middle is selected for accumulating the acoustic wave energy inside the mR tube. The length (l_0) and width (w_0) (l_0, w_0, see Fig. 1(c)) of the side slit are chosen to well couple acoustic energy into the gap between two QTF prongs with a width of 0.3 mm (shown in Fig. 1(a)). Microresonator center is positioned below the QTF tips, and the distance from the QTF tips to the mRs' axis is 0.7–1.0 mm [22,23,26] (shown in Fig. 1(b)). In order to improve the sensitivity of OB-QEPAS-based sensor, a modified mR (shown in Fig. 1(d)) was made to reduce the viscous drag [27,28] between the mR and the QTF so as to keep the QTF assembled into OB-QEPAS spectrophone to work with a high Q factor ($Q \sim 8000$), because the subsequent signal to noise ratio (SNR) of the sensor is directly proportional to $\sqrt{Q}$. But the modification to mR for forming the modified mR does not change the basal acoustic characteristics of the mR tube. And the resonant frequency of the mR with a side slit in the middle is noted as f_{mR}. The optimum OB-QEPAS spectrophone configuration is to make acoustic coupling between QTF and mR to be the best, namely sets $f_{mR}=f_0$. Therefore, in real applications, designing optimum mR parameters to keep $f_{mR}=f_0$ is an effective method to acquire the best sensitivity of OB-QEPAS-based sensor. In the following section, a theoretical model will be presented to give a method to obtain the optimum mR parameters of this "off beam" configured sensor.

In the case where the cross-sectional dimensions of an acoustic resonator are much smaller than the acoustic wavelength, the excited acoustic wave can be described by a one-dimensional acoustic field along the length of the resonator [10]. In QEPAS, the used mR (with a diameter ≤ 1.50 mm in comparison with an acoustic wavelength of $\lambda \sim 10.5$ mm at atmosphere and room temperature) can thus be treated as a one-dimensional acoustic resonator, only the first longitudinal acoustic resonance occurs inside the mR tube. Presently, there are mainly six prototypes of one-dimensional acoustic resonator to be usually used in acoustic instruments (shown in Fig. 2(a)–2(f)), which refer to open–open tube (Fig. 2(a)), close–close tube Fig. 2(b), open–close tube (Fig. 2(c)) [10]; open–open tube with an orifice in the middle (Fig. 2(d)), wide open–partly open tube (Fig. 2(e)), full close–partly open tube (Fig. 2(f)) [29,30], respectively. In the later sections, we will investigate the acoustic impedance at two open ends and the side slit of open–open tube with a side slit (treated as an orifice) (shown in Figs. 2(d) and 3(a)) in the middle used in OB-QEPAS for theoretical analysis of the resonant condition of

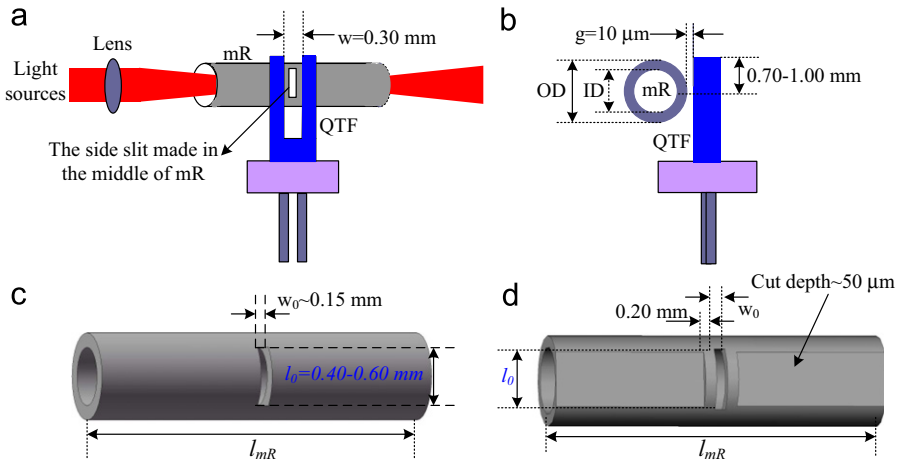

Fig. 1. Configuration of OB-QEPAS spectrophone and the used mR tube. OB-QEPAS spectrophone profile: (a) seen from the side slits of the mR; (b) seen from the mR' axis; (c) the 3D (3 dimensions) map of the mR tube with a side slit in the middle; (d) the 3D map of the modified mR.

this type of tube. And then the optimum tube length as a function of acoustic velocity, inner diameter (ID), and the acoustic conductivity of the side slits of mR can be calculated with the theory of end correction.

2.1. Acoustic impedance-determination the resonant condition of mR

In OB-QEPAS-based sensor, a one-dimension tube called mR with a length l_{mR} (in mm), outer diameter (OD) and inner diameter (ID) (see Fig. 3(a)) was used to enhance the detection sensitivity of the sensor. As shown in Fig. 3(b), considering a mR tube of effective length L_{eff} (in mm) and cross-sectional area S (in mm^2) filled with gaseous fluid, the acoustic pressure inside the mR can be described by the acoustic transmission line theory [9,10]:

$$P(x,t) = A\exp(i(\omega t - kx)) + B\exp(i(\omega t + kx)) \quad (1)$$

where x is the position coordinate (shown in Fig. 3(b), the origin of the coordinate axis is noted as 0), $k=\omega/\upsilon=2\pi f/\upsilon$ the wave number, f the sound frequency (in Hz) and υ the acoustic wave propagation velocity inside the resonator (in m/s), i the unit of imaginary. The constants A and B stand for the amplitude of acoustic pressure, which are determined by acoustic boundary conditions. And the corresponding particle velocity of the gaseous fluid inside the mR was given by [9,10,30–32]

$$u(x,t) = -\frac{1}{\rho}\int \delta\left(\frac{\partial P(x,t)}{\partial x}\right)dt, \quad (2)$$

where ρ is the density of the gaseous fluid inside the mR.

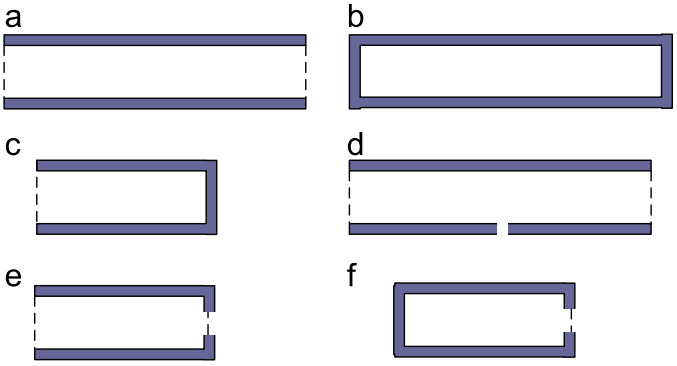

Fig. 2. Several prototypes of one-dimension acoustic resonator adopted in PAS.

Acoustic impedance Z inside the mR, expressed as [9,10,30–32]

$$Z = \frac{P(x,t)}{Su(x,t)}; \quad (3)$$

where Z represents a complex value that is the ratio of the complex $P(x,t)$ to the complex particle velocity of the gaseous fluid $u(x,t)$ at a cross section area of S where the acoustic pressure is applied.

Because the acoustic pressure inside the mR excited by modulated light satisfies the Eq. (1), the optimum mR parameters can be determined through analysis of the acoustic impedances at mR's two ends and the side slit in the middle. According to the theory outlined in [10,30–32], in the case of finite mR, if the value of the input acoustic impedance at $x=0$ is recorded as $Z(0)$, using Eqs. (1–3), $Z(0)$ can be given by

$$Z(0) = \frac{\rho\upsilon}{S}\frac{A+B}{A-B} \quad (4)$$

And the acoustic impedance $Z(L_{eff})$ at $x=L_{eff}$ is expressed as

$$Z(L_{eff}) = \frac{\rho\upsilon}{S}\frac{A\exp(-ikL_{eff})+B\exp(ikL_{eff})}{A\exp(-ikL_{eff})-B\exp(ikL_{eff})} \quad (5)$$

where L_{eff} is the effective length of the mR including its two ends corrections [30]. Eliminating A and B by combination Eqs. (4) and (5) yield

$$Z(L_{eff}) = \frac{Z(0)-(i\rho\upsilon/S)\tan(kL_{eff})}{(SZ(0)/(i\rho\upsilon))\tan(kL_{eff})+1} \quad (6)$$

For OB-QEPAS spectrophone configuration, adopted the theory outlined in [30], the mR can be seen as a tube with an orifice in the middle (referred as "mR with an orifice in the middle" shown in Fig. 3(a)), the acoustic impedance of the side slit was recorded as Z_s; if the value of the input acoustic impedance at $x=0$ was recorded as Z_{a0}, the acoustic impedance at $x=a$, at the left side of the side slit is Z_a and at the right side of the side slit is Z_{b0}, the acoustic impedance at $x=L_{eff}$ ($a+b=L_{eff}$) is Z_b (shown in Fig. 3(b)), and the continuity equation holds at the side slit in the middle of the mR is given by [14,30–32]:

$$Z_a = \frac{Z_{a0}-(i\rho\upsilon/S)\tan(ka)}{(SZ_{a0}/(i\rho\upsilon))\tan(ka)+1} \quad (7)$$

$$\frac{1}{Z_a} = \frac{1}{Z_s} + \frac{1}{Z_{b0}} \quad (8)$$

$$Z_b = \frac{Z_{b0}-(i\rho\upsilon/S)\tan(kb)}{(SZ_{b0}/(i\rho\upsilon))\tan(kb)+1} \quad (9)$$

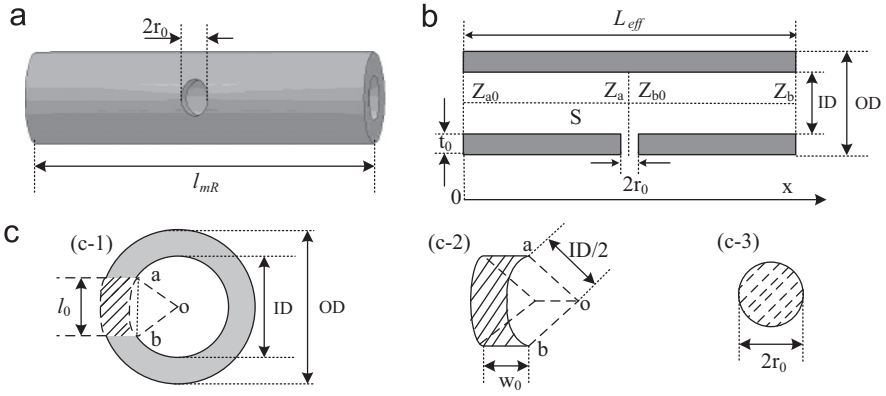

Fig. 3. Theoretical model of mR with a side slit in the middle. (a) the theoretical model of 3D map of a tube with an circular orifice in the middle; (b) the cross section profile of mR along mR' axis and the center of the orifice, the coordinate system and the acoustic impedance at two ends and the side slit of mR; (c) the acoustic conductivity of the side slit in the middle of mR tube: $\sigma_s=s_s/t_{eff}$, (c-1) The length and thickness of the arc-shaped side slit, (c-2) The surface area district of the side slit and the slit width (see from mR' axis at the cross section area district in the middle of mR), (c-3) The surface area district of the side slit equals to a circular with the same districts area and the radius of the circular is r_0.

when acoustic resonance occurs inside the mR [30], $Z_b=Z_{a0}=0$, as a result, combined Eqs. (7–9), we can deduce that

$$\cot(ka)+\cot(kb)=-\frac{i\rho\upsilon}{S}\frac{1}{Z_s} \tag{10}$$

For the side slit, its acoustic impedance can be given by [30]:

$$Z_s=\frac{i\rho\upsilon k}{\sigma_s} \tag{11}$$

σ_s is the acoustic conductivity of the side slit (treated as a side hole) and it can be determined as follows [30]:

$$\sigma_s=\frac{s_s}{t_{\text{eff}}} \tag{12}$$

where s_s, t_{eff} are the surface area and the effective thickness of the side slit, respectively. t_{eff} can be determined by adding the real mR's wall thickness to two ends corrections of the side slit.

And taking into account that the side slit is in the middle of the mR ($a=b=L_{\text{eff}}/2$), Eq. (10) can be reduced to

$$2\cot(k\frac{L_{\text{eff}}}{2})=-\frac{\sigma_s}{kS} \tag{13}$$

2.2. End correction-calculation the effective thickness of the side slit and the physical length of the mR

Due to the fact of the mismatch between the one dimensional acoustic wave inside the mR tube and the three dimensional field (of spherical wave front) radiated from the opening end of the mR to free space [10], end corrections for mR's two ends and interior and outer ends of the side slit should be performed. The end corrections result in a longer effective length than its real physical length. The theories of end corrections given in [10,29–32] were adopted to calculate the effective lengths.

The side slit can be equivalent to a circular side hole with the same area (shown in Fig. 3(a)). As a matter of fact, circular side hole is a tube with diameter of $2r_0$ and real physical length of t_0 (which equals to the real mR's wall thickness). Taking into account that the side hole was drilled on the outer arc-shaped wall surface of the mR, two ends of the side hole can be seen as unflanged [10,30–32]. And two ends corrections to equivalent circular side hole thickness t_0 is $1.20r_0$, and thus t_{eff} can be written as follows [10,30–32]:

$$t_{eff}=t_0+1.2r_0 \tag{14}$$

where t_0 stands for mR's wall thickness, $t_0=(OD\text{-}ID)/2$ (see Fig. 3(b) and 3(c)), r_0 for the equivalent hole radius.

In reality, the side slit is not circular (Fig. 1(c)), it is a slit with the width of w_0 and the arc length of l_s (Fig. 3(c-1) and 3(c-2)), the side hole radius r_0 should be derived from the district s_s of an equivalent circular hole (Fig. 3(c-3), dash area):

$$r_0=\sqrt{\frac{s_s}{\pi}}=\sqrt{\frac{w_0 l_s}{\pi}} \tag{15}$$

where l_s is the length of the arc $\overset{\frown}{oab}$ (Fig. 3(c-1) and 3(c-2)), l_s can not be directly measured in the experiment, but the circle chord $\overline{ab}=l_0$ can be measured (Fig. 1(c)). As a result, l_s can be deduced as follow:

$$l_s=\text{ID}\arcsin\left(\frac{l_0}{\text{ID}}\right) \tag{16}$$

The same as two ends corrections of the circular side hole, two ends of the mR are also unflanged [10,30–32], ends corrections to the real physical length l_{mR} of the mR is $1.2R$, so that we can acquire that

$$l_{mR}=L_{eff}-1.2R \tag{17}$$

Using Eqs. (12–17), the optimum mR length (l_{mR}, mm) can be expressed as follows in a function of mR's inner radius (R=ID/2 mm), the acoustic velocity inside the mR (υ, m/s), the QTF resonant frequency ($f_0=f_{\text{mR}}$, Hz), and the acoustic conductivity (σ_s, mm) of the side slit in the middle of the mR:

$$l_{\text{mR}}=\frac{\upsilon}{f_0}-\frac{\upsilon}{\pi f_0}\arctan\left(\frac{4\pi S}{\sigma_s}\cdot\frac{f_0}{\upsilon}\right)-1.2R \tag{18}$$

Thus the physical length (l_{mR}) of the mR with a side slit in the middle can be determined through Eqs. (12–18).

2.3. Comparison mR with AR

Finally, the mR used in QEPAS was compared to the acoustic resonator (AR) excited in its first longitudinal mode adopted in conventional PAS [9]. For AR, the length (l_{AR}, mm), inner diameter (D=ID=$2r$, mm), resonant frequency (f_{AR}, Hz) and acoustic velocity (υ, m/s) inside the AR satisfy the following Eqs. [9,10,33]:

$$l_{AR}=\frac{\upsilon}{2f_{AR}}-1.7r \tag{19}$$

Differences and connections between the mR used in QEPAS and the AR adopted in traditional PAS were investigated through theoretical analysis with our model and the related acoustic transmission line theory [9,10] and the results were compared with experiments measurements given in published papers [22,23].

Otherwise, according to results given in [31–33], the acoustic velocity (υ, m/s) of general gas, given in Eq. (20), depends on the mol mass of molecular (M, kg/mol) and the absolute temperature (T) in Kelvin (K), and the specific heat ratio of the gas constant (γ):

$$\upsilon=\sqrt{\frac{\gamma RT}{M}} \tag{20}$$

where R=8.3144 J/(mol K) is the universal gas constant. For ambient air, the acoustic velocity can be approximately expressed as follow in a function of centigrade temperature (C, °C) [32]:

$$\upsilon(C)=331.6+0.6C(m/s) \tag{21}$$

3. Results and discussions

3.1. Experimental results

Our former experiments have committed to investigate the performance of OB-QEPAS-based sensor by detection of water vapor at ambient atmospheres and temperature changing from 12 to 25 °C. The optimum mR lengths with respect to IDs, ODs, the side slits, acoustic velocities (υ) inside the mR, and resonant frequencies of QTF (f_0) and the mR (f_{mR}), were experimentally obtained [22,23] and the experiments measurements were summarized in Table 1.

Table 1
Optimum mRs' lengths acquired by theoretical calculations via different mRs' parameters compared with experimental results given in [22,23].

Type of mR	Experiment measurements parameters (mm)						Optimum length (mm)		υ (m/s)
	OD	ID	t_0	l_0	w_0	σ_s	l_{exp}	l_{theor}	
mR1	0.70	0.45	0.13	0.40	0.15	0.24	8.00	8.02	345
mR2	1.20	0.80	0.20	0.60	0.15	0.24	5.84	5.97	340
mR3	1.30	0.90	0.20	0.60	0.15	0.24	5.24	5.62	339
mR4	1.80	1.50	0.15	0.60	0.15	0.26	5.00	4.81	347
mR5	0.80	0.50	0.15	0.50	0.15	0.31	8.00	8.06	345

ID, OD, l_0, w_0 and l_{exp} were measured by vernier caliper with uncertainty of 0.02 mm.

3.2. Theoretical calculations and simulations

In order to evaluate the feasibility of the theoretical model, theoretical simulations and calculations were used to analyze the mR used in OB-QEPAS spectrophone configuration. The values of the acoustic velocities (υ) were calculated using Eq. (21) and the calculated results were given in Table 1. Because the changing value of resonant frequency of QTF (f_0) is only within 4 Hz in our experiments, f_0 can be approximately seen as a constant for theoretical calculations and simulations. And thus the best sensitivity of OB-QEPAS-based sensor mainly lies on the mR parameters. Using Eq. (18) and the experimentally measured parameters listed in Table 1, the optimum mRs' (referred to mR1–mR5) lengths versus different IDs, acoustic velocities ($\upsilon = 339-347$ m/s), and the acoustic conductivities of the side slits can be acquired through theoretical calculations. The calculations were listed in Table 1 for comparison with experiments measurements [22–23]. Finally, the dependence of the optimum mR's lengths on inner radiuses (R=ID/2), acoustic velocities, and acoustic conductivities of the side slit applied for mR1–mR5 was simulated by using Eq. (18) with $200\ \text{m/s} \le \upsilon \le 500\ \text{m/s}$, $\sigma_s \approx 0.26$ mm, and $0.15\ \text{mm} \le R \le 0.8\ \text{mm}$. The simulated results with 3D photograph were shown in Fig. 4.

3.3. Side-by-side comparison of theory and experiments

For the numerical calculated results given in Table 1, the average deviation of 2.9% is in the order of the measurement accuracy. Therefore the agreement can be considered very well. The main source of deviation between the theoretical results (l_{theor}) and the experiments measurements (l_{exp}) mainly originated from the measurement deviation of the mR parameters including OD, ID, and the length (l_0) and the width (w_0) of the side slit, which lead to an uncertainty in the length of the mR. Otherwise, although the theory of finger-holes in woodwind instruments was used to roughly determine the optimum length of mR5 (its parameters given in Table 1) at 1 atm and room temperature, the results show that our theoretical model is more helpful for designing the mRs' parameters compared with experiments measurements [23].

For the theoretical simulations shown in Fig. 4, compared it with the experimentally determined equation [22]:

$$\frac{ID}{l_{mR}} = -0.04546 + 0.232^{*}ID \tag{22}$$

The 3D simulation photograph maybe more accurately reflects the fact that the optimum mRs' lengths not only depend on IDs, but also on acoustic velocities inside the mR. And the simulations also show that the acoustic velocity inside the mR plays a very important role in designing the optimum mR parameters. As a result, it is necessary to discuss the effect of acoustic velocity on the performance of OB-QEPAS-based trace gas sensors.

According to our theoretical model, the acoustic velocity in a specified gas is a function of temperature and mol mass. Mostly widespread trace gas sensing applications, various targeted trace gas species with different concentrations mixed in various buffer gases types, at different temperatures, will be detected by OB-QEPAS-based sensors. And targeted trace gas species mixed with buffer gases, at different temperatures, result in different acoustic velocities inside the mR. The targeted gas concentrations were in the range of ppmv (part per million by volume) to ppbv (part per billion by volume) for most applications of trace gas detection, the volume ratio of buffer gases were more than 99.99%. Seen from Eq. (20), it is a fact that buffer gases determine

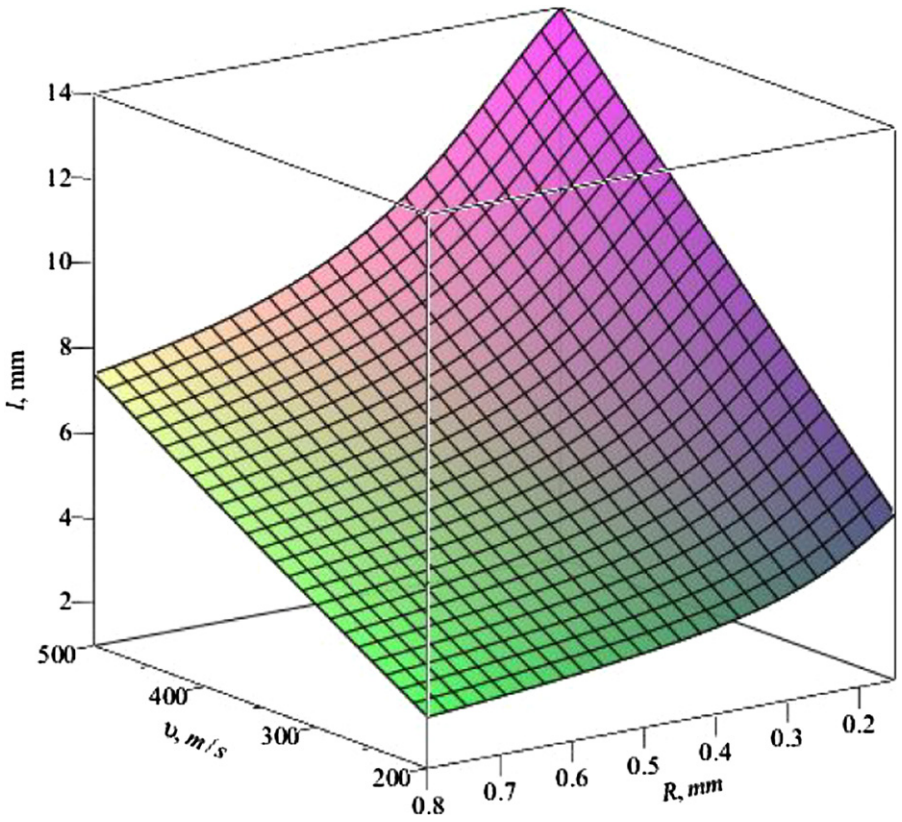

Fig. 4. With the frequency f_0=32.750 kHz and $\sigma_s \approx 0.26$ mm, the 3D photograph of the optimum mR length ($l=l_{\text{mR}}$) dependence on its inner radius (R) ranging from 0.15 mm to 0.75 mm and acoustic velocity (υ) in the range of 200 m/s to 500 m/s was theoretically simulated.

the acoustic velocity inside the mR. With the former experimental results and experiences [33], zero air, nitrogen (N_2), oxygen (O_2), helium (He) and argon (Ar) were commonly chosen as buffer gases in PAS-based sensor. And the parameter values of these buffer gases were given in Table 2 for theoretical calculation. In order to better match the mR and QTF (setting $f_{mR}=f_0$), buffer gases with different types and volume ratio can be used to change the acoustic velocity so that f_{mR} can be shifted to coincide with the resonant frequency of QTF f_0 [34], or the influence of acoustic velocity on the performance of OB-QEPAS-based sensor that assembled with the mR with settled parameters including OD, ID, and the side slit should be studied for calibrating the QEPAS signal to acquiring the correct concentration of targeted trace gas species [34].

3.4. The relation between the mR used in QEPAS and the AR adopted in conventional PAS

The investigative methods for mR enhanced OB-QEPAS given in the former section can also be applied to analyze the mR in "on beam" and "half on beam" QEPAS spectrophone configuration. In the former paper [21], we have proved that the optimized mR parameters in "half on beam" can be approximately applied to that in "on beam" (because the two mR tubes have the same parameters in "on beam") through experimental and theoretical analysis. As a matter of fact, the mR used in on beam and half on beam is the prototype of open–partly open tube shown in Fig. 2(e), we called it "orifice ended mR". The theoretical analysis about the mR used in on beam, half on beam (Fig. 2(e)), and "off beam" (Fig. 2(d)) were compared to the AR adopted in conventional PAS [9,10] (Fig. 2(a)–2(c)), and the differences and relationship among them were presented in the following sections.

The resonant condition of "orifice ended mR" can be described as follow [21]:

$$\tan(kL_{\text{eff}})+\frac{kS}{\sigma_o}=0 \tag{23}$$

Where σ_o, d_o, are the acoustic conductivity and orifice diameter of partly open end, respectively, *ID* is the inner diameter of the "orifice ended mR", and σ_o can be determined by [21]:

$$\sigma_o=d\left(1+\frac{d}{ID}\right)^{1.19} \tag{24}$$

Table 2
Physical constants of several carrier gases at 1 atm pressure with temperature of 20 °C. And υ is calculated using Eq. (20) in the former section.

Substance	ρ_0 (kg m^{-3})	γ	M (kg mol^{-1})	υ (m/s)
N_2	1.25	1.401	0.0280	349
O_2	1.43	1.398	0.0320	326
Zero air	1.293	1.402	0.0288	344
He	0.178	1.63	0.0040	996
CO_2	1.98	1.293	0.0440	268

When partly open end of "orifice ended mR" becomes completely closed ($d=0$), and thus $\sigma_o=0$ in Eq. (23). As a result, Eq. (23) can be reduced to

$$\cot(kL_{\text{eff}})=0 \text{ or } L_{\text{eff}}=\frac{n\lambda}{4}|_{n=1}=\frac{\lambda}{4} \tag{25}$$

which is used to describe the first longitudinal mode resonance of the open–closed tube shown in Fig. 2(c) [10].

Similarly, if partly open end of "orifice ended mR" becomes wide open, that is to say there is no orifice at the partly open end [21], "orifice ended mR" becomes to open–open tube working with the first longitudinal mode resonance (Fig. 2(a)) [10]. The effective length satisfies the following equation:

$$\tan(kL_{eff})=0 \text{ or } L_{eff}=\frac{m\lambda}{2}|_{m=1}=\frac{\lambda}{2} \tag{26}$$

Therefore, the optimum mR length (l_{mR}) in "on beam" and "half on beam" QEPAS satisfied the relation $\lambda/4<l_{mR}<\lambda/2$, which is also consistent with the theory of traditional PA cell.

For mR used in OB-QEPAS, as can be seen that, if $a=l$, $b=0$, and the side hole is pisitioned at one end of the mR (this end is partly open) in Eq. (10), Eq. (10) will change to Eq. (23) which is used to describe the resonance of "orifice ended mR". As a result, a tube with a side hole in the middle becomes to a tube ended with an infinitely thin orifice at partly open end [21]. Similarly, if the side hole does not exist, $\sigma_s=0$ in Eq. (13), and then Eq. (13) will change to Eq. (26) which corresponds to the first longitudinal mode resonance of the open–open tube (shown in Fig. 2(a)) [10]. And those differences and connections between the AR adopted in traditional microphone based PAS and the mR used in QEPAS were also summarized in Table 3.

In summary, with the theoretical model, we can deeply understand the performance of OB-QEPAS-based sensor device, especially the mR used in QEPAS, and also can use the theoretical results to design and optimize the sensor for improving its sensitivity so as to satisfy our real applications.

4. Conclusions

A systematical theory has been introduced to investigate the OB-QEPAS-based sensor performance. The optimum mR parameters dependence on other variables, especially the resonant frequency of QTF, the acoustic velocity inside the mR tube, was studied through theoretical analysis. And the influence of the acoustic velocity on OB-QEPAS-based sensor performance was theoretically investigated in combination with the related experimental measurements. The introduced theory about the mR used in on beam, half on beam, and off beam QEPAS was compared to the acoustic resonator excited in its first longitudinal mode adopted in conventional PAS and the relationship among them was presented after theoretical analysis. With this theoretical model, we can design the mR with better geometrical parameters for systematic optimization of OB-QEPAS-based sensor.

Table 3
N_2 or zero air is chosen as carrier gases at 1 atm pressure with temperature of 20 °C, the parameters of the microresonator (mR) used in off beam (mR-a) and on beam (mR-b) QEPAS were compared with the acoustic resonator (AR) excited in its first longitudinal mode in conventional PAS.

Tube	ID (mm)	OD (mm)	υ (m/s)	f (kHz)	λ (mm)	Optimum length (mm)
mR-a	0.40–1.50	0.70–1.80				$\lambda/4<l_{mR}<\lambda$
mR-b	0.40–1.00	0.70–1.30	~345	~32.750	~10.53	$\lambda/4<l_{mR}<\lambda/2$
AR	~3–30	seen as ∞		~1–2	~86–173	$l_{AR}\sim\lambda/2-0.85*ID$

Acknowledgments

This research was supported by National Natural Science Foundation of China (NSFC) (Foundation No.41175036) and the Natural Science Foundation provided of Anhui province of China (Foundation No.11040606M147). The support of the Groupement de Recherche International SAMIA between CNRS (France), RFBR (Russia), and CAS (China) is acknowledged, too.

References

[1] A. Rosencwaig, Photoacoustics and Photoacoustic Spectroscopy, Wiley, New York, 1980.
[2] P. Hess, Resonant Photoacoustic Spectroscopy, Vol. 111 of Current Topics in Chemistry, Springer-Verlag, Berlin, 1983.
[3] Z. Bozkia, A. Pognyb, G. Szabb, Applied Spectroscopy Reviews 46 (2011) 1.
[4] A.A. Kosterev, F.K. Tittel, D.V. Serebryakov, A.L. Malinovsky, I.V. Morozov, Review of Scientific Instruments 76 (2005) 043105.
[5] E.L. Holthoff, D.A. Heaps, P.M. Pellegrino, IEEE Sensors Journal 10 (2010) 572.
[6] J. Saarela, J. Sand, T. Sorvajrvi, A. Manninen, J. Toivonen, Sensors 10 (2010) 5294.
[7] T. Kuusela, J. Kauppinen, Applied Spectroscopy Reviews 42 (2007) 443.
[8] C.F. Dewey Jr., R.D. Kamm, C.E. Hackett, Applied Physics Letters 23 (1973) 633.
[9] F.G.C. Bijnen, J. Reuss, F.J.M. Harren, Review of Scientific Instruments 67 (8) (1996) 2914.
[10] A. Miklós, P. Hess, Z. Bozóki, Review of Scientific Instruments 72 (4) (2001) 1937.
[11] B. Baumann, B. Kost, H.G. Groninga, M. Wolff, Review of Scientific Instruments 77 (2006) 044901.
[12] B. Kost, B. Baumann, M. Germer, M. Wolff, M. Rosenkranz, Applied physics B 102 (2011) 87.
[13] A.A. Kosterev, Y.A. Bakhirkin, R.F. Curl, F.K. Tittel, Optics Letters 27 (2002) 1902.
[14] A.A. Kosterev, F.K. Tittel, Applied Optics 43 (2004) 6213.
[15] S. Schilt, A.A. Kosterev, F.K. Tittel, Applied Physics B 95 (2009) 813.
[16] L. Dong, A.A. Kosterev, D. Thomazy, F.K. Tittel, Proceedings of SPIE 7945 (2011) 50R.
[17] D. Weidmann, A.A. Kosterev, F.K. Tittel, N. Ryan, D. McDonald, Optics Letters 29 (2004) 1837.
[18] R. Lewicki, G. Wysocki, A.A. Kosterev, F.K. Tittel, Optics Express 15 (2007) 7357.
[19] H. Yi, K. Liu, W. Chen, T. Tan, L. Wang, X. Gao, Optics Letters 36 (2011) 481.
[20] L. Dong, A.A. Kosterev, D. Thomazy, F.K. Tittel, Applied Physics B 100 (2010) 627.
[21] H. Yi, W. Chen, X. Guo, W. Zhang, S. Sun, K. Liu, T. Tan, X. Gao, Applied Physics B (2012), http://dx.doi.org/10.1007/s00340-012-4988-7.
[22] K. Liu, X. Guo, H. Yi, W. Chen, W. Zhang, X. Gao, Optics Letters 34 (2009) 1594.
[23] K. Liu, H. Yi, A.A. Kosterev, W. Chen, L. Dong, L. Wang, T. Tan, W. Zhang, F.K. Tittel, X. Gao, Review of Scientific Instruments 81 (2010) 103103.
[24] S. Böttger, M. Angelmahr, W. Schade, Photoacoustic gas detection with LED QEPAS, in: CLEO/Europe and EQEC 2011 Conference Digest, OSA Technical Digest (CD) (Optical Society of America, paper CH_P14, 2011.
[25] W. Schippers, E. Gershnabel, J. Burgmeier, O. Katz, U. Willer, I.S. Averbukh, Y. Silberberg, W. Schade, Applied Physics B 105 (2011) 203.
[26] N. Petra, J. Zweck, A.A. Kosterev, S.E. Minkoff, D. Thomazy, Applied Physics B 94 (2009) 673.
[27] S.L. Firebaugh, F. Roignant, E.A. Terray, Modeling the response of photoacoustic gas sensors, in: Proceedings of Comsol Conference 2009, Newton, MA, Oct. 8–10, 2009.
[28] S.L. Firebaugh, F. Roignant, E.A. Terray, Enhancing sensitivity in tuning fork photoacoustic spectroscopysystems, in: Proceedings of the Sensor Application Symposium (SAS), IEEE Press, New York, 23–25 Feb. 2010, p. 30.
[29] A.T. Jones, Journal of the Acoustical Society of America 12 (1941) 387.
[30] E.G. Richardson, Technical aspects of sound: sonic range and airborne sound, Elsevier Pub. Co., Amsterdam; New York, 1957, pp. 12, 487.
[31] L.E. Kinsler, A.R. Frey, Fundamentals of acoustics, John Wiley & Sons, Inc, New York London, 1962, pp. 116, 186.
[32] D.R. Raichel, The science and applications of acoustics, Springer Science+Business Media, Inc., 233 Spring Street, New York, NY 10013, USA, 2006, pp. 131.
[33] J.P. Besson, S. Schilt, L. Thevenaz, Spectrochimica Acta Part A 60 (2004) 3449.
[34] L. Dong, K. Liu, A.A. Kosterev, F.K. Tittel, Effect of Speed of Sound on Quartz-Enhanced Photoacoustic Spectroscopy Trace Gas Sensor Performance, in: CLEO: 2011-Laser Applications to Photonic Applications, OSA Technical Digest (CD) (Optical Society of America), paper CThCC, 2011.